

Numerical study of a dual-PCM thermal energy storage unit with an optimized low-volume fin structure

M. Mozafari ^{a,*}, Kamel Hooman ^b, Ann Lee ^a, Shaokoon Cheng ^a

^a School of Engineering, Macquarie University, NSW 2109, Australia

^b School of Mechanical and Mining Engineering, The University of Queensland, QLD 4072, Australia



ARTICLE INFO

Keywords:

Phase change material
Energy storage
Consecutive charging-discharging
Dual-PCM
Fin
Optimization

ABSTRACT

Phase Change Materials (PCMs) are widely used as storage mediums in latent thermal energy storage systems and are useful to tackle the inconsistencies in energy supply and demand associated with renewable energy resources. However, weak thermal conductivity is the major disadvantage of PCMs, as they cause slow charging and discharging of thermal energy storage systems. The performance enhancement of a unique thermal energy storage unit design that consists of two PCMs and with optimized fins is demonstrated in the current study. Different arrangements of dual-PCMs are first examined by comparing the overall charging-discharging time. The proposed dual-PCM layout for a horizontal double-pipe energy storage unit, not demonstrated in existing work, reduces the total charging-discharging time by 13.6% compared with the conventional single-PCM case. Results from this study further show that applying nanoparticles is less effective than adding fins for the proposed dual-PCM design configuration. Adding nanoparticles to the dual-PCM design results in 2.2 times shorter charging-discharging time, while the proposed design with fins incorporated results in a remarkable 7.6-fold improvement in charging-discharging time. To further enhance the performance of the energy storage unit, response surface methodology (RSM) is used to predict the optimum fin angles, and results show that fins tilted at 51.1° and 42.6°, measured clockwise from the upper middle section and counter-clockwise from the lower middle section, respectively, reduced the total charging-discharging time by 7.5%. This article exemplifies a systematic approach to designing a high-performance LTES system that leverages the combined benefits of multiple PCMs and optimized fin design.

1. Introduction

Global energy demand is growing exponentially [1], and this will indubitably result in many environmental problems, such as air pollution and climate change, from the increased global use of fossil fuels. Solar energy is a sustainable, clean, renewable energy source that can help resolve the above predicament. However, the inconstant availability of solar energy is a critical drawback, and this could be aided by innovative designs of thermal energy storage (TES) systems [2]. Latent thermal energy storage (LTES) is a common type of heat storage system which utilises phase change materials (PCMs). LTES systems have been widely used in solar-based units such as domestic solar hot water systems to save and store excess energy during peak sun hours. PCMs have exceptional capabilities to store and release thermal energy during their phase changes, which is a property that has resulted in their widespread use, not limited to TES systems [3,4] but also in other applications such

as electronics cooling [5,6], battery thermal management [7,8], and other types of thermal systems [9–12]. The thermal processes related to the effectiveness of charging and discharging latent heat storage units will be examined in this study.

Several heat transfer enhancement techniques have been proposed to improve the thermal response of LTES systems, such as the usage of extended surfaces and fins [13–15], porous matrices [16], and nanoparticles [17]. Pizzolato et al. [18] utilized a topology optimization method to create an efficient finned layout for a shell-and-tube LTES system and demonstrated that the fin structures with geometrical dimensions optimised for melting are not necessarily useful and applicable to optimise solidification. Nakhchi et al. [19] optimised stepped fins to improve the melting performance of PCM in a LTES systems. They examined different orientations of stepped fins with different step ratios and subsequently demonstrated that stepped fin designs generally have better performances than the conventional design with horizontal fins. Guo et al. [20] employed angled fins to improve the melting

* Corresponding author.

E-mail address: ryan.mozafari@hdr.mq.edu.au (M. Mozafari).

| Nomenclature | |
|----------------------|--|
| C | mushy zone constant |
| C_p | specific heat (J/kg K) |
| d | diameter (m) |
| g | gravity acceleration (m/s ²) |
| h | specific enthalpy (J/kg) |
| k | thermal conductivity (W/m K) |
| k_B | Boltzmann constant (J/K) |
| L | latent heat of fusion (J/kg) |
| P | pressure (Pa) |
| S | momentum source term (N/m ³) |
| t | time (s) |
| T | temperature (K) |
| T_l | liquidus temperature [K] |
| T_s | solidus temperature [K] |
| u | velocity in r direction (m/s) |
| v | velocity in θ direction (m/s) |
| r | radial coordinate |
| <i>Greek symbols</i> | |
| ρ | density (kg/m ³) |
| β | thermal expansion coefficient (K ⁻¹) |
| μ | dynamic viscosity (kg/ms) |
| θ | angular coordinate |
| δ | constant small number |
| λ | liquid-fraction |
| ϕ | volume fraction |
| ζ | correction factor |
| <i>Subscripts</i> | |
| i | inner tube |
| $init$ | initial |
| l | liquid PCM |
| np | nano particle |
| o | outer shell |
| ref | reference |
| s | solid PCM |
| <i>Acronyms</i> | |
| CCD | consecutive charging and discharging |
| DOE | design of experiment |
| FVM | finite volume method |
| HTF | heat transfer fluid |
| LTES | latent thermal energy storage |
| NEPCM | nano particle enhanced PCM |
| PCM | phase change materials |
| PRESTO | pressure staggering option |
| SIMPLE | semi-implicit method for pressure linked equations |
| TES | thermal energy storage |

performance of PCM in a shell-and-tube TES system. The study demonstrated that tilting the fins by a small angle regardless of the direction of the tilt results in an anisotropic melting process, with a 10° downward tilting of fins reducing the overall melting time of the system by as much as 55.41 %. In addition to the above, the use of non-rectangular fins is also likely able to improve the performance of a thermal energy storage unit. In a numerical study, Sharma et al. [21] investigated a tube-in-tank storage unit where water (as PCM) was placed outside a tube filled with refrigerant. They conducted an optimization study to study the number of longitudinal fins needed to result in a fast-freezing process. The design configuration that constituted 15 fins was identified as the optimum case that could increase the heat transfer rate by 15 %. Yao et al. [22] showed that triangular fin arrangement increases solidification time by 31 % compared to the conventional design with rectangular fins. Their results also showed that increasing the fin length can significantly decrease the discharging time, while using very thin fins reduces the efficiencies of the TES.

Recently, some researchers have introduced novel metal structures to facilitate the melting and solidification of PCMs in thermal energy storage. Zheng et al. [23] numerically studied different configurations of tree-shaped fins (with two to four branch levels) on the solidification performance of PCM in a TES unit. It was discovered that the heat storage unit with four-level tree-shaped fins provides the fastest solidification rate and the most uniform solidification process. Mahdi et al. [24] utilized fin-assisted foam strips to enhance the rate of melting and solidification in a shell-and-tube storage unit. The foam strips were preferred over full foam as they facilitate natural convection of liquid PCM and occupy lesser volume leading to higher storage capacity. It was discovered that uneven fins with foam strips enhanced the melting and solidification rates by 58 % and 42 %, respectively. In a numerical study, Huang et al. [25] introduced a hierarchical metal structure (when tree-shaped branches are grown in downward direction) to improve the melting performance of PCM in a horizontal TES system. It was reported that a hierarchical fin structure reduces the melting time by 35.9 % and provides better performance compared with a tree-shaped fin.

Based on the above studies, extended surfaces and fins are purportedly useful to improve the LTES system, albeit having the potential

caveat of resulting in low storage density, high total system weight and high cost of production and maintenance. These effects may be minimised using a minimal volume fraction of the thermal enhancers with a cost-effective and highly manufacturable design, which is a subject of investigation in this current work.

Indeed, improving the thermal response of a TES system has been the goal of many current research and development activities. Another way to address the issue is to use multiple phase change materials. For example, Mozafari et al. [5] showed that combining two PCMs could increase the operating time of a thermal management system by up to 12 % compared to a single PCM. Mahdi et al. [26] investigated the potential effects of PCMs layout and arrangements in a multiple-PCM system on solidification. The effects of cascaded metal foams and the inclusion of nanoparticles were also investigated therein. It was found that the use of multiple PCMs with cascaded metal foam leads to the best performance, where the solidification time was reduced by 94 % compared to the baseline case, which consisted of a single PCM. Siyabi et al. [27] studied how the arrangement of multiple PCMs in a shell-and-tube thermal energy storage unit may affect heat transfer rate. Their results showed that applying multiple PCMs results in higher average temperature and shorter melting time than those with a single PCM. Mozafari et al. [28] demonstrated how features of a dual-PCM design could be optimised to accelerate their solidification in a shell-and-tube heat exchanger. The study showed that PCM arranged eccentrically can shorten the solidification time by up to 15 % compared with the conventional single PCM system. A further study [29] showed that applying multiple PCMs integrated with nanoparticles can also significantly improve the simultaneous charging and discharging of a triplex-tube energy storage system. Mozafari et al. [2] further showed that a dual-PCM design could also be effectively applied in a triplex-tube energy storage unit to improve its charging and discharging performances. Taken together, the advantage that multiple PCM brings to a TES system is compelling and irrefutable. However, there remains a need to clarify how multiple (or dual) PCMs could be arranged in a horizontal double-pipe energy storage unit to accelerate both charging and discharging cycles. Furthermore, how the aforementioned specific design configuration could be potentially enhanced through the integration of fins is

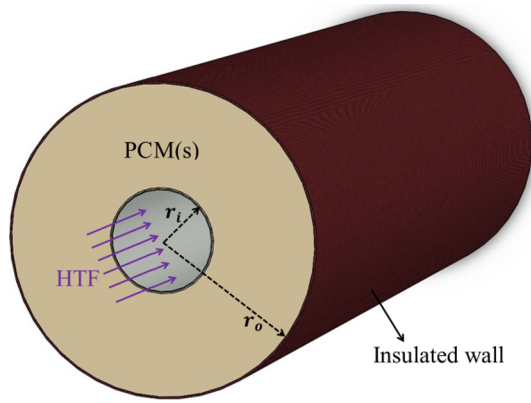


Fig. 1. The TES unit used in the current study.

also unclear. The key novelty of this work is that an efficient dual-PCM arrangement is introduced that facilitates both melting and solidification processes.

This paper investigates the effects of different dual-PCM arrangements in consecutive charging and discharging cycles of a horizontal double-pipe thermal energy storage unit. Specifically, this current work aims to shed light on the creative design of thermal energy storage systems and shows how combining an well-dual-PCMs layout with an optimized low-volume fin structure can remarkably improve the

charging-discharging performance of the system. The above has not been expounded in published research to the best of the authors' knowledge.

2. Physical model

Fig. 1 illustrates the graphical representation of the TES applied in this study. This TES system consists of two concentric aluminium pipes, where $r_i = 25.4\text{mm}$, and $r_o = 75\text{mm}$. This tubular heat storage unit has been used as a PCM container in existing literature [30–33]. Unfluctuating conditions of the HTF passing through the inner pipe were modelled by prescribing a constant temperature at the wall. A single PCM model and 5 different arrangements of dual PCM (as shown in Fig. 2) designs placed within the annulus are investigated. Three different phase change materials with different melting points were chosen and described in Table 1. The PCMs were selected such that the average properties of dual PCMs (PCM-1 and PCM-3) were nearly equal to those of the single PCM (PCM-2) presented in Table 1. The most efficient configuration was eventually selected and used as the base unit in the subsequent studies to investigate the effects of adding nanoparticles or fin structures. Therefore, the properties of the aluminium oxide nanoparticles and metal fins are also provided in Table 1.

The five dual-PCM configurations are presented in Fig. 2. Case-1 is the case that consists of a single PCM (PCM-2 or RT-60) which is used as a benchmark for the other dual-PCM cases. To model the charging process, the inner pipe was assumed to be heated, and this was represented by prescribing a constant temperature of 353 K uniformly on the

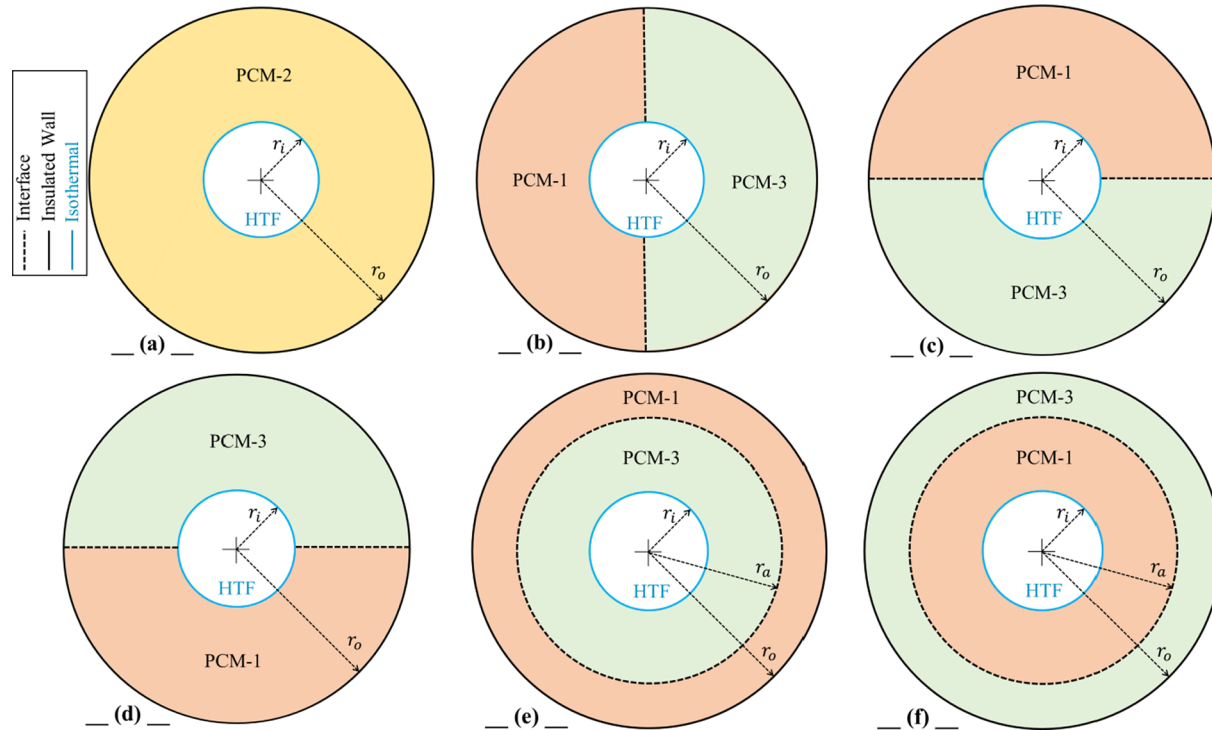


Fig. 2. Computational domains of the storage unit in the present work; (a) case-1, (b) case-2, (c) case-3, (d) case-4, (e) case-5, (f) case-6.

Table 1
Properties of applied materials in this study [34].

| Material | $k[\text{W/m.K}]$ | $C_p[\text{KJ/Kg.K}]$ | $L[\text{KJ/Kg}]$ | $T_s[\text{K}]$ | $T_l[\text{K}]$ | $\rho[\text{Kg/m}^3]$ | $\mu[\text{N.s/m}^2]$ |
|-------------------------|-------------------|-----------------------|-------------------|-----------------|-----------------|-----------------------|-----------------------|
| PCM-1 (RT-55) | 0.2 | 2 | 170 | 324 | 330 | 770 | 0.0264 |
| PCM-2 (RT-60) | 0.2 | 2 | 160 | 328 | 334 | 770 | 0.0288 |
| PCM-3 (RT-65) | 0.2 | 2 | 150 | 331 | 338 | 770 | 0.03 |
| Al_2O_3 | 36 | 0.765 | — | — | — | 3600 | — |
| Aluminium | 202.4 | 0.87 | — | — | — | 2719 | — |

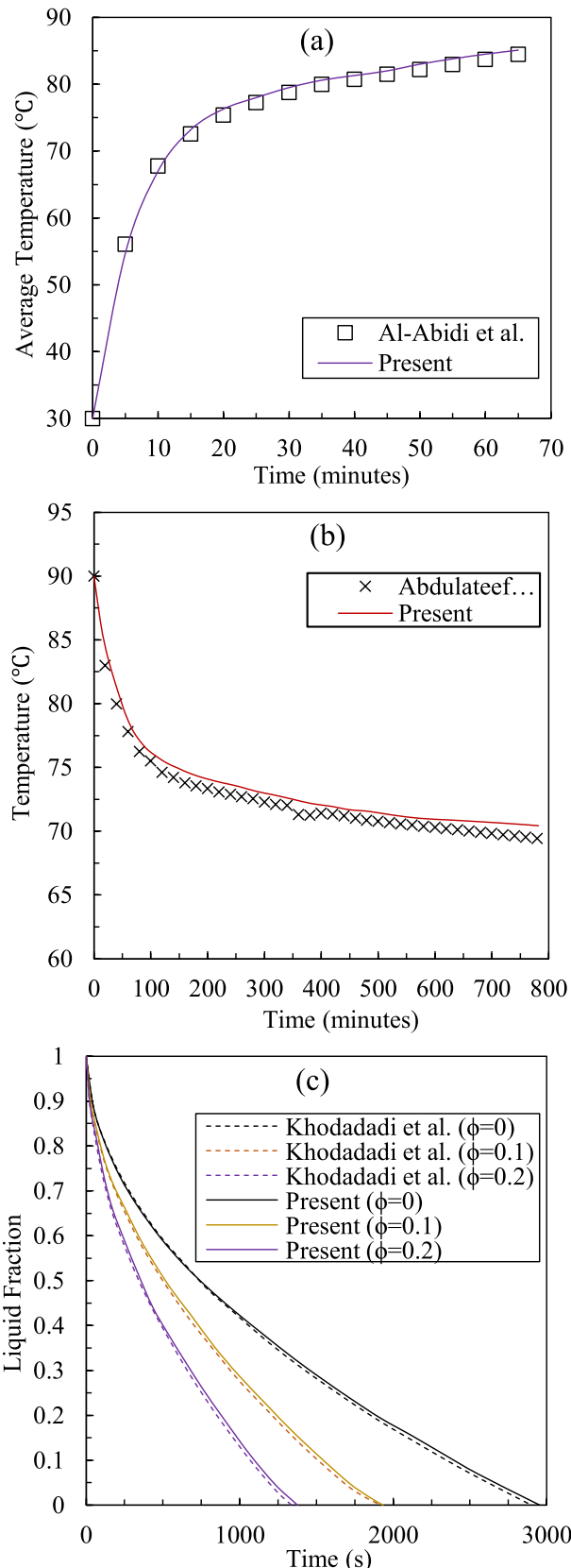


Fig. 3. Validation of the current numerical method against the results reported by: (a) Al-Abidi et al. [30], (b) Abdulateef et al. [46], and (c) Khodadadi et al. [45].

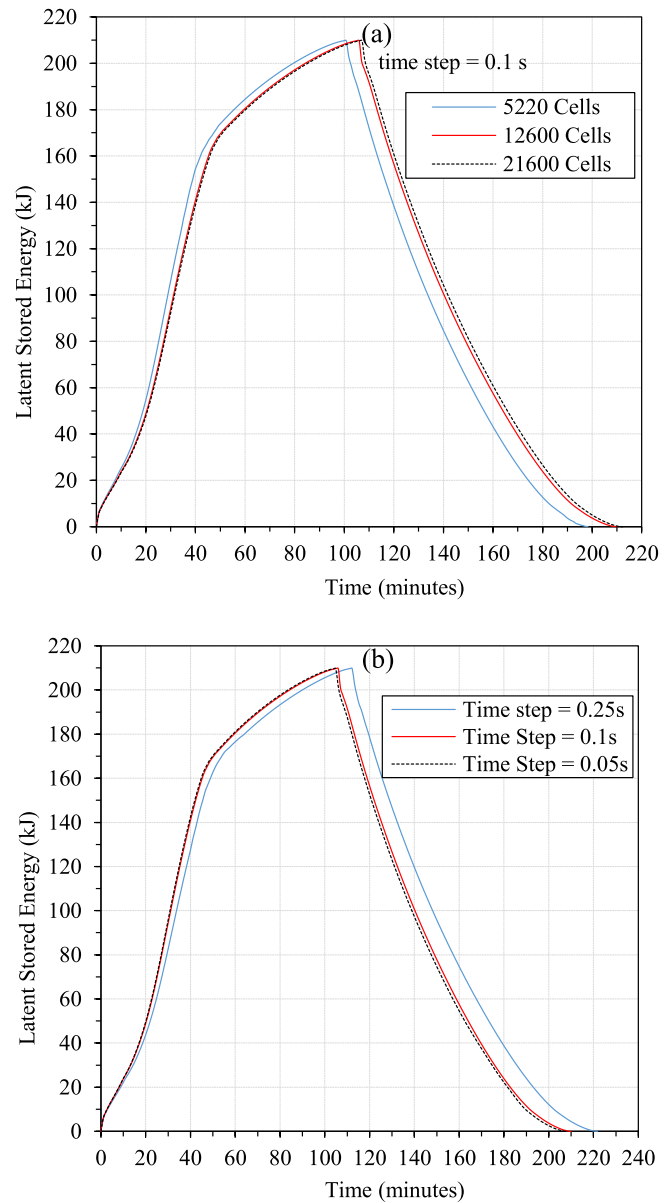


Fig. 4. Effects of (a) grid size, and (b) time step on the transient prediction of stored latent energy.

surface of the pipe. When the whole PCM is completely melted, the discharging process commences when the wall temperature assumes a constant temperature of 300 K. The outer shell of the TES was assumed to be thermally insulated. To provide a meaningful comparison between the dual-PCM cases, the volume of the PCMs in each design was ensured to be equal between the cases.

3. Numerical model

3.1. Initial and boundary conditions

Unsteady-two-dimensional modelling was conducted to predict the phase change behaviour of the PCMs. Three-dimensional simulation is unnecessary in this simulation, given that the cross section is constant and the results of the physical phenomena in the out of plane direction are identical, as demonstrated in some existing work [26,29,30,33,35].

The effect of natural convection motion in the liquid PCM was considered. Initially, the unit was assumed to be fully solidified ($T_{initial} = 300K$) and the initial condition could be expressed as:

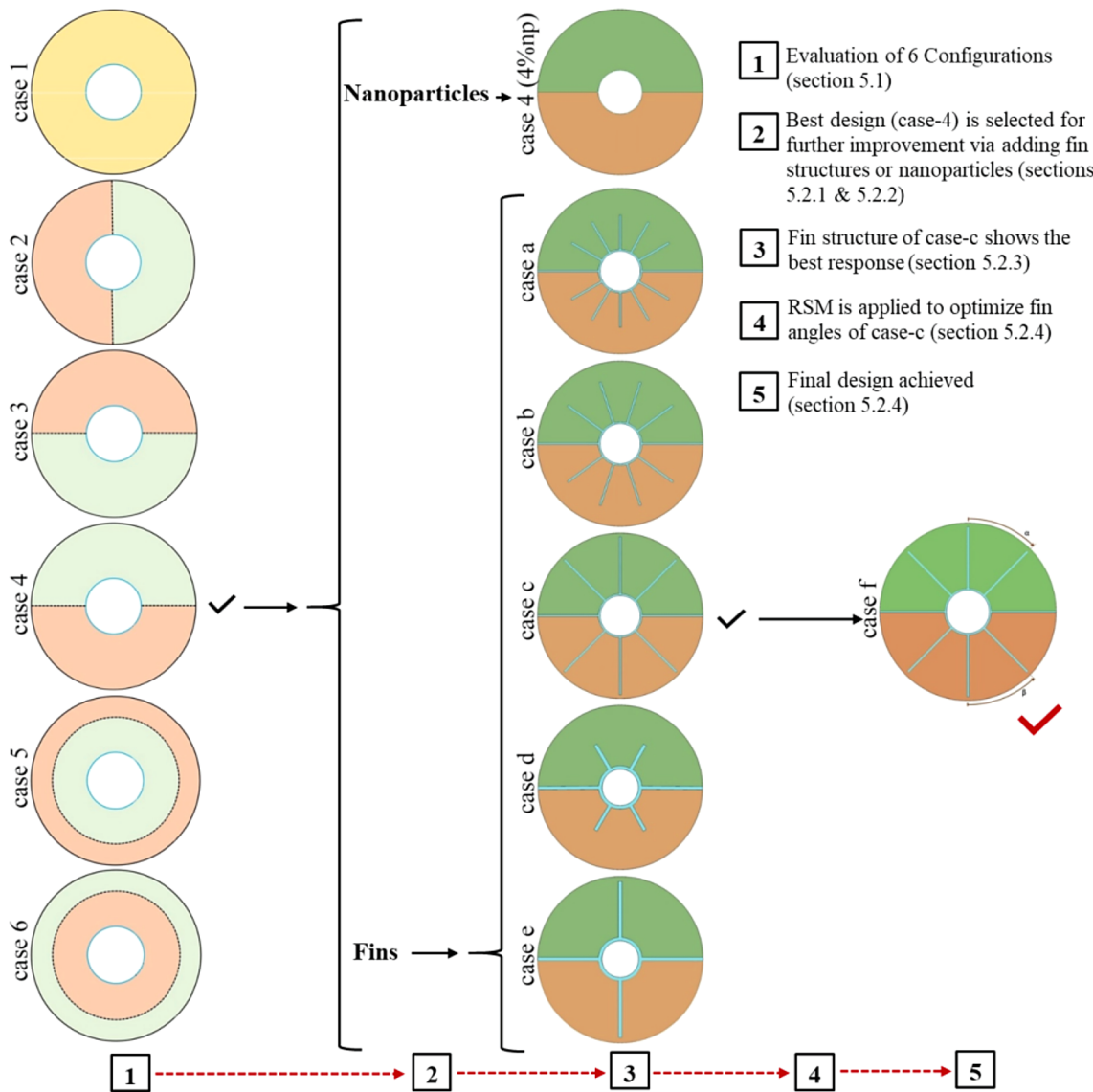


Fig. 5. The design development flowchart of the present study.

$$t = 0 \rightarrow u_r = 0, u_\theta = 0 \text{ & } T = T_{init} = 300 K$$

The boundary conditions could be expressed as follows:

$$r = r_i \rightarrow u_r = 0, u_\theta = 0, T = T_{HFT} \begin{cases} = 353 K \text{(for charging)} \\ = 300 K \text{(for discharging)} \end{cases}$$

$$r = r_o \rightarrow u_r = 0, u_\theta = 0, \frac{\partial T}{\partial r} = 0 \quad (2)$$

$$\theta = \pm\pi/2 \rightarrow \frac{\partial u_r}{\partial \theta} = 0, u_\theta = 0, \frac{\partial T}{\partial \theta} = 0 \quad (\text{cases 1, 3, 4, 5 \& 6})$$

The following interface conditions are implemented at wall borders:

$$\text{border walls} \begin{cases} T_{PCM(i)} = T_{PCM(i+1)} \\ u_r = 0 \\ u_\theta = 0 \end{cases} \quad (3)$$

According to the abovementioned equation, the rate of heat leaving the $(i)_{th}$ PCM layer across the interface is the same as the rate of heat entering the $(i+1)_{th}$ layer along the same direction.

3.2. Assumptions

The following assumptions were made in the models:

- (1) 1. The liquid PCM was assumed to be incompressible, Newtonian, and laminar flow.
2. Thermal radiation heat transfer was ignored inside the TES.
3. The expansion and contraction of PCMs during melting and solidification were considered minimal and insignificant.
4. The properties of the tube wall and fins were assumed isotropic and homogeneous.
5. Heat transfer fluids were assumed to have a constant temperature.
6. Temperature variations of HTFs were considered insignificant.
7. The no-slip assumption was made along the solid boundaries

3.3. Governing equations

Momentum, mass, and energy conservation equations, as demonstrated below, were employed to solve the problem:

(I) Mass conservation.

$$\nabla \cdot V = 0 \quad (4)$$

(II) Momentum conservation.

$$\rho \left(\frac{\partial u_r}{\partial t} + V \cdot \nabla u_r \right) = - \nabla P + \mu \nabla^2 u_r + \rho g \sin \theta + S_{u_r} \quad (5)$$

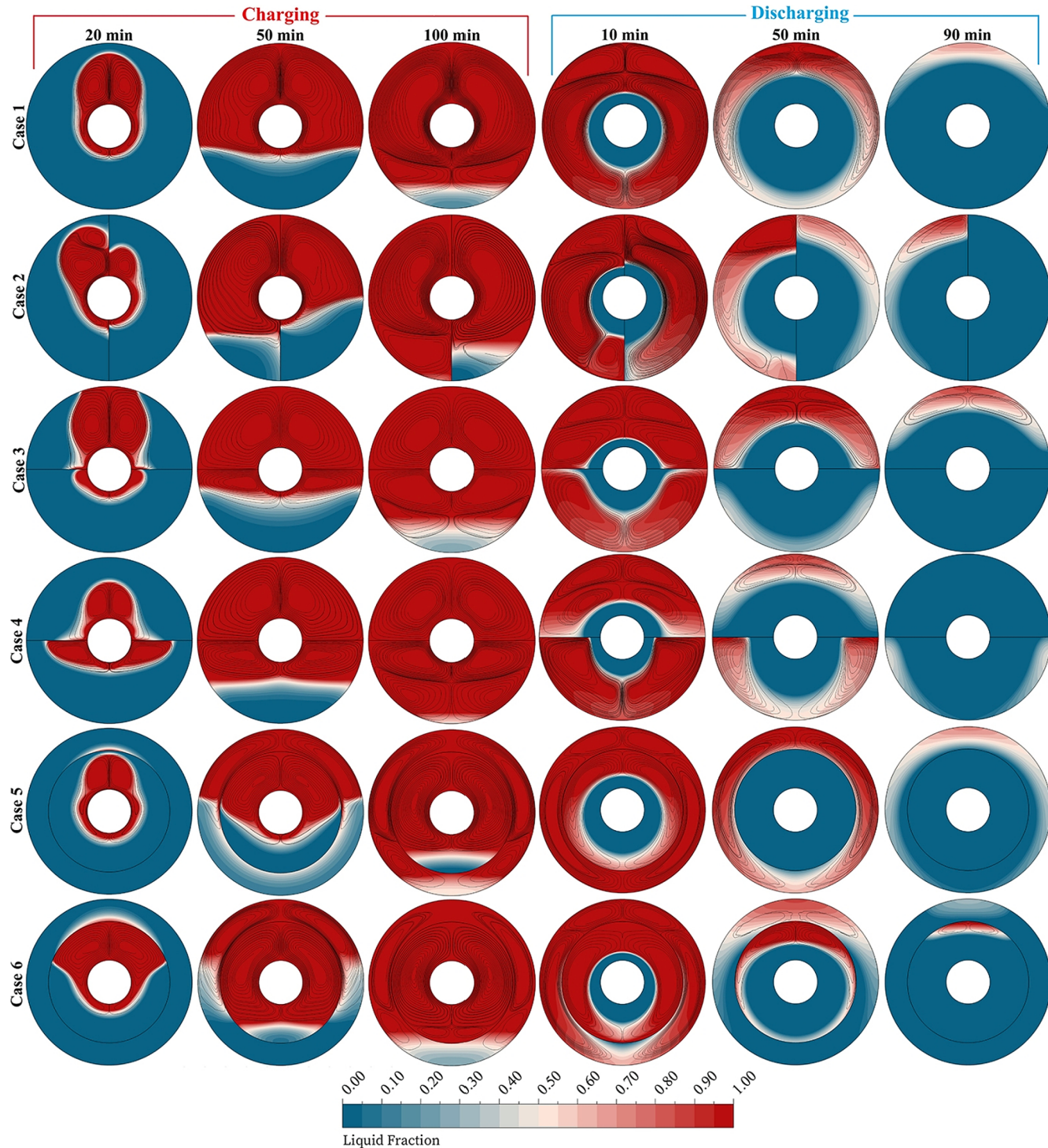


Fig. 6. Evolutions of solid–liquid interface and streamlines in charging and discharging process for all cases.

$$\rho \left(\frac{\partial u_\theta}{\partial t} + V \cdot \nabla u_\theta \right) = - \nabla P + \mu \nabla^2 u_\theta + \rho g \cos \theta + S_{u_\theta} \quad (6)$$

(III) Energy conservation.

$$\frac{\partial}{\partial t} (\rho H) + \nabla \cdot (\rho VH) = \nabla \cdot (k \nabla T) \quad (7)$$

Here, ($H = h + \Delta H$) where h is sensible enthalpy and ΔH is latent heat. Momentum sink could also be presented as:

$$S_{u_r} = -C(1-\lambda)^2 \frac{u_r}{\lambda^3 + \delta} \quad (8)$$

$$S_{u_\theta} = -C(1-\lambda)^2 \frac{u_\theta}{\lambda^3 + \delta} \quad (9)$$

The mushy zone constant (C) is fixed as 10^5 kg/sm^3 following previous studies [36–38]. $\delta = 0.001$ was assumed to ensure a non-zero value in the denominator. The sensible enthalpy can be calculated as:

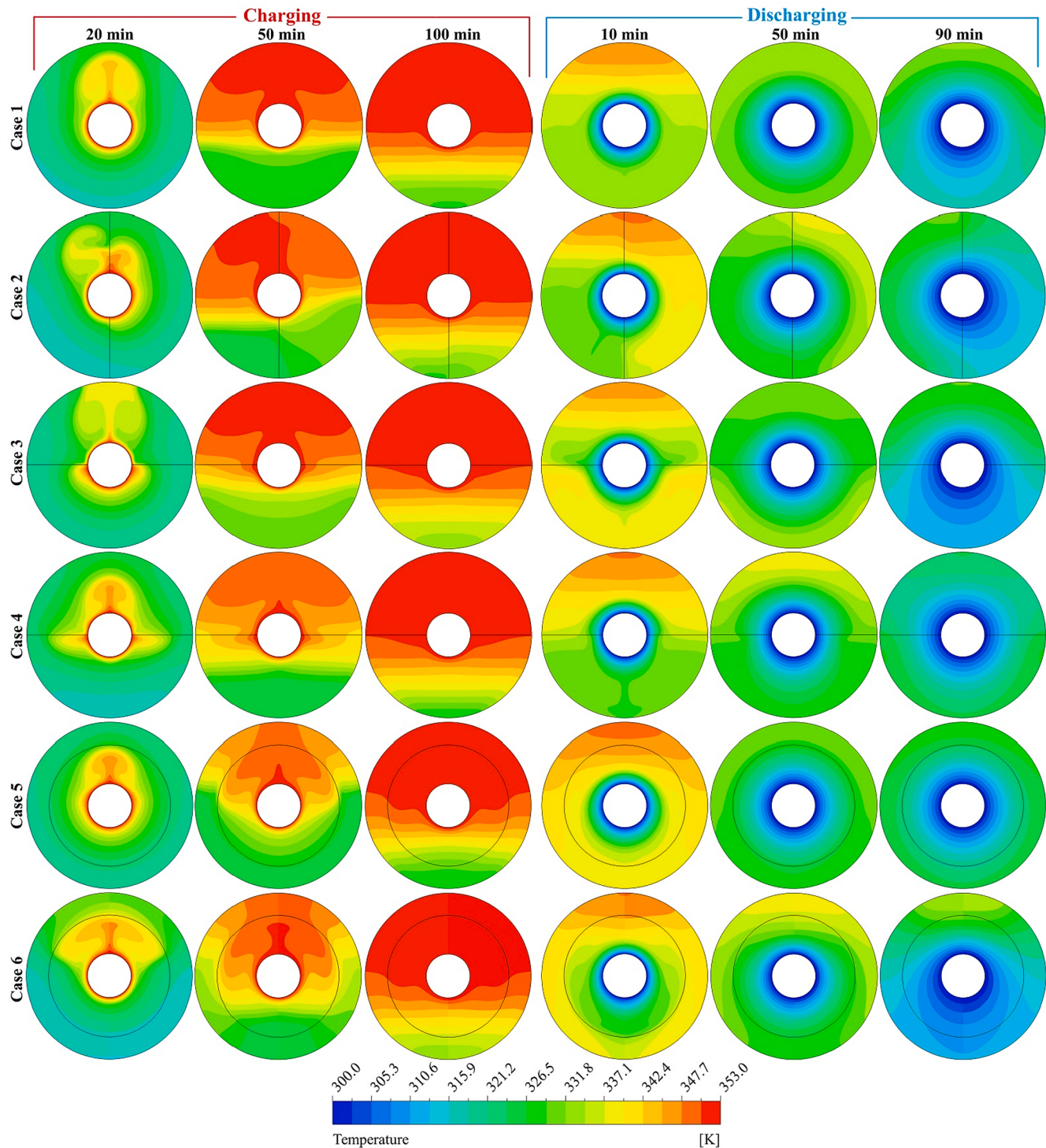


Fig. 7. Evolutions of isotherms in the charging and discharging process for all of the six cases.

$$h = h_{ref} + \int_{T_{ref}}^T C_p dT \quad (10)$$

In the abovementioned equation, h_{ref} is the reference enthalpy at ($T_{ref} = 273\text{K}$). The latent heat capacity could be determined as:

$$\Delta H = \lambda L \quad (11)$$

Where λ is the liquid fraction of PCM, which could be determined based on the solidus and liquidus temperatures ($T_s < T < T_l$):

$$\lambda = \begin{cases} 0, & T \leq T_s \\ \frac{T - T_s}{T_l - T_s}, & T_s < T < T_l \\ 1, & T \geq T_l \end{cases} \quad (12)$$

Boussinesq approximation was employed to take into account the effect of natural convection in the liquid PCM, where the density of the liquid phase could be presented as:

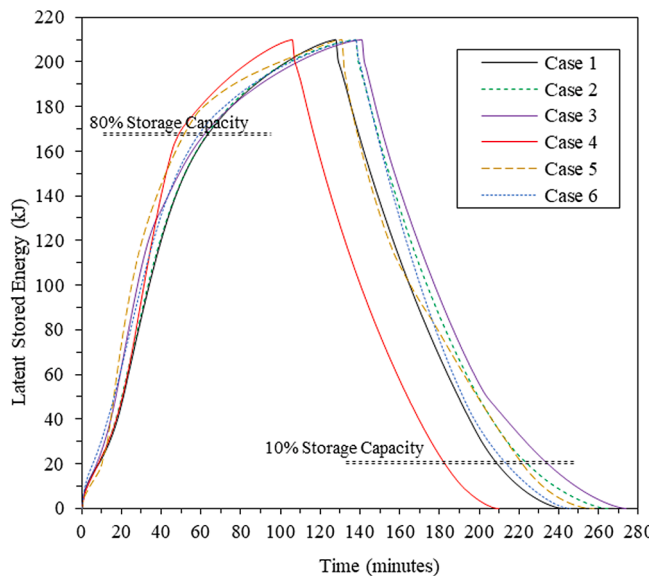


Fig. 8. Stored latent energy in consecutive charging and discharging for all cases.

$$\rho = \frac{\rho_m}{\beta(T - T_m) + 1} \quad (13)$$

Where ρ_m denotes the original density of liquid PCM, β is the thermal expansion coefficient, and $T_m = (T_s + T_l)/2$. T_s and T_l are the solidus and liquidus temperatures, respectively.

3.4. Thermophysical properties of nanoparticle enhanced PCMs

Table 1 presents the thermophysical properties of Al₂O₃ nanoparticles, and the applied PCMs obtained from manufacturer [34]. The mixture method was implemented for the properties of the nanoparticle enhanced PCM (NEPCM) as below:

$$\rho_{nepcm} = (1 - \phi_{np})\rho_{pcm} + \phi_{np}\rho_{np} \quad (14)$$

$$(\rho C_p)_{nepcm} = (1 - \phi_{np})(\rho C_p)_{pcm} + \phi_{np}(\rho C_p)_{np} \quad (15)$$

$$(\rho L)_{nepcm} = (1 - \phi_{np})(\rho L)_{pcm} \quad (16)$$

$$(\rho\beta)_{nepcm} = (1 - \phi_{np})(\rho\beta)_{pcm} + \phi_{np}(\rho\beta)_{np} \quad (17)$$

Where ϕ_{np} is the volumetric concentration of nanoparticles. The dynamic viscosity and thermal conductivity of the NEPCM could be determined following the models suggested by Vajjha and Das [39,40], respectively as:

$$\mu_{nepcm} = 0.983e^{(12.959\phi)}\mu_{pcm} \quad (18)$$

$$\begin{aligned} k_{nepcm} = & \frac{k_{np} + 2k_{pcm} - 2\phi_{np}(k_{pcm} - k_{np})}{k_{np} + 2k_{pcm} + \phi_{np}(k_{pcm} - k_{np})} + \\ & 5 \times 10^4 \beta_k \zeta \phi_{np} \rho_{pcm} (C_p)_{pcm} \sqrt{\frac{k_B T}{\rho_{np} d_{np}}} f(T, \phi_{np}) \end{aligned} \quad (19)$$

k_B is Boltzmann constant ($k_B = 1.381 \times 10^{-23}$ J/K), $\beta_k = 8.4407(100\phi_{np})^{-1.07304}$, and f can be expressed as:

$$\begin{aligned} f(T, \phi_{np}) = & (2.8217 \times 10^{-2}\phi_{np} + 3.917 \times 10^{-3}) \frac{1}{T_{ref}} \\ & + (-3.0669 \times 10^{-2}\phi_{np} - 3.9112 \times 10^{-3}) \end{aligned} \quad (20)$$

This model includes the size of nanoparticles, and f is the correction factor related to the Brownian motion of nanoparticles. ζ is considered equal to the liquid-fraction (λ) in Eq. (12) since there is no Brownian motion in the solid phase [41]. d_{np} represents the diameter of nanoparticles, and T_{ref} represents the reference temperature ($T_{ref} = 298$ K) [39]. RT60 (PCM-2) is considered as the reference PCM in the current study.

3.5. Numerical procedure

The current study aims to simulate PCM's sequential charging and discharging in the TES system by applying a transient two-dimensional model. The enthalpy-porosity approach [42] was adopted to compute the melting and solidification of PCM, wherein the porosity in each cell is set equal to the liquid fraction in that cell. Finite-Volume Method (FVM) with high-order quadratic upstream interpolation for QUICK scheme [43] was used to discretize the governing equations. The PRESSURE BASED method was adopted to solve the governing

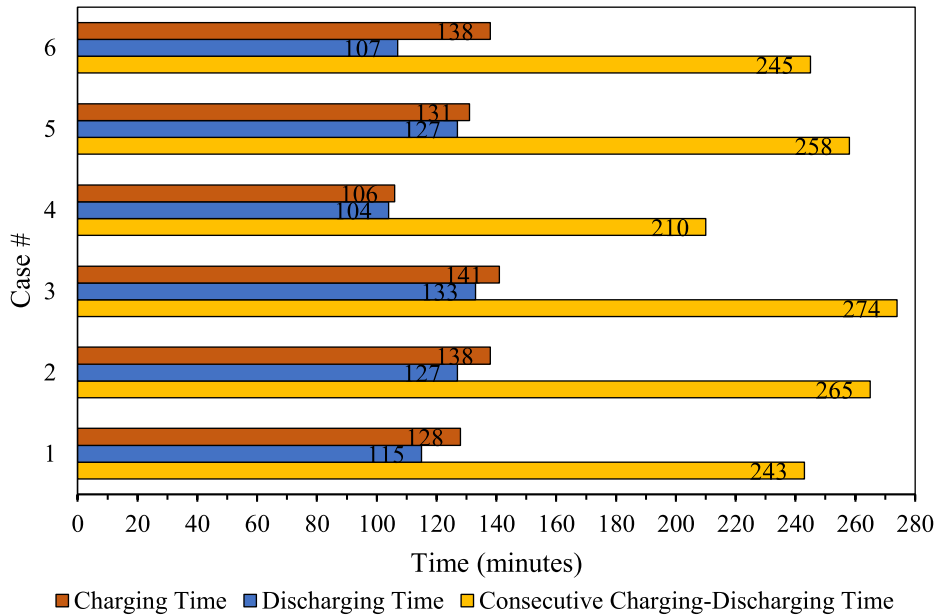


Fig. 9. Charging and discharging times for different cases.

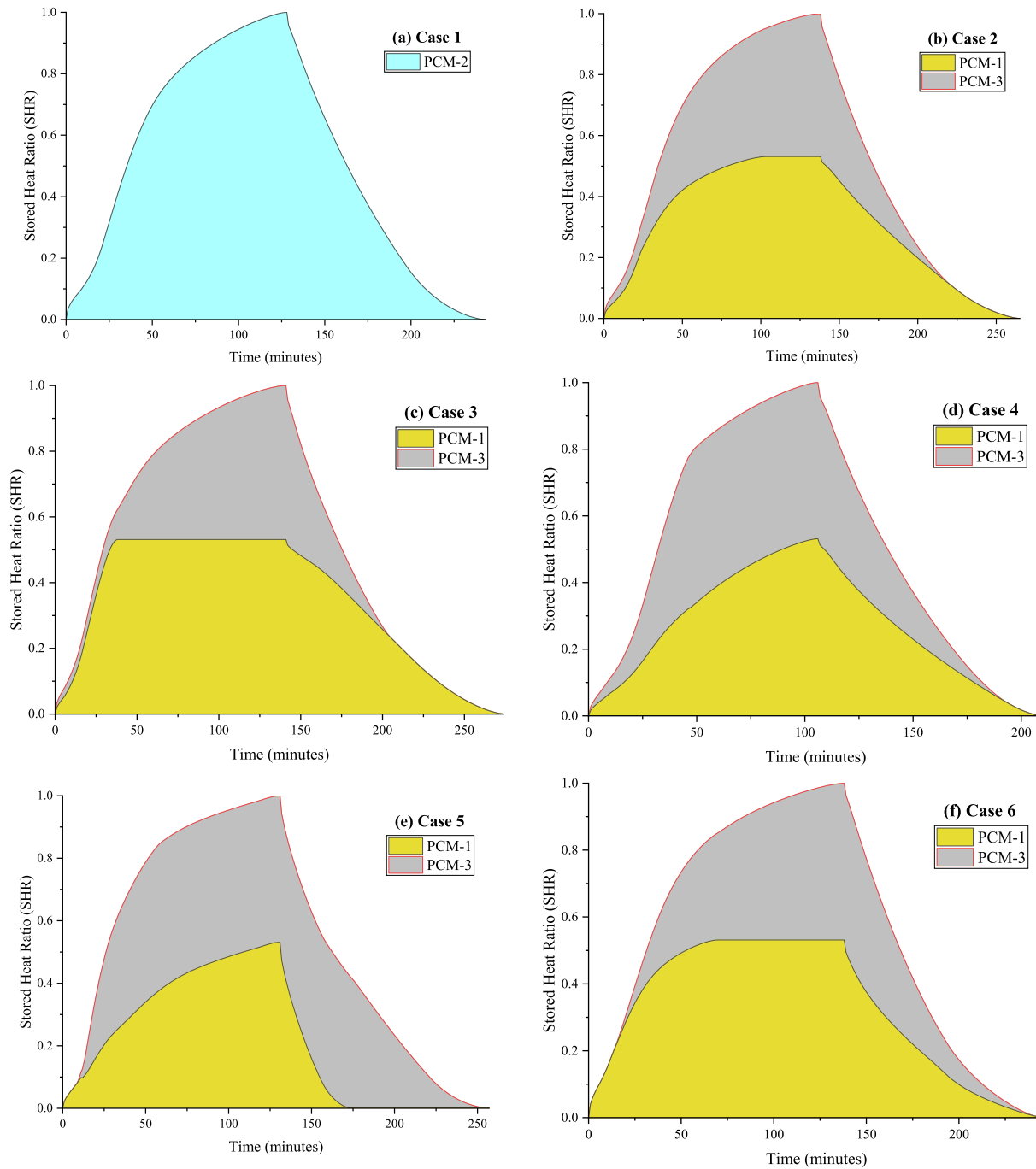


Fig. 10. Temporal variation of SHR for all single-PCM and dual-PCM cases.

equations. The pressure staggering option (PRESTO) scheme was utilized for pressure correction during the iterative solution process. Semi-implicit method for pressure linked equations (SIMPLE) algorithm recommended by Patankar [44] was also used in pressure–velocity coupling. The under-relaxation factors were 0.5, 0.3 and 1 for the momentum, pressure, and energy, respectively. Termination of the simulations based on the convergence criteria is set as 10^{-4} for continuity and momentum, and 10^{-6} for thermal energy.

4. Validation and verification

4.1. Numerical methodology validation

The numerical method has been validated against the data of three

published studies. Specifically, the applied materials' thermo-physical properties and their initial and boundary conditions were prescribed the same as existing studies [30,45,46] to verify the numerical model.

4.1.1. Validation of the model in the melting process

The current numerical model is validated by the experimental results reported by Al-Abidi et al. [30], where the melting of RT82 occurred in a triplex tube heat exchanger. Fig. 3(a) shows that the transient average temperature can be accurately predicted using the current numerical solver.

4.1.2. Validation for solidification enhancement with fins

The experimental data reported by Abdulateef et al. [46], pertinent to the solidification of RT82 in a triplex-tube heat exchanger with

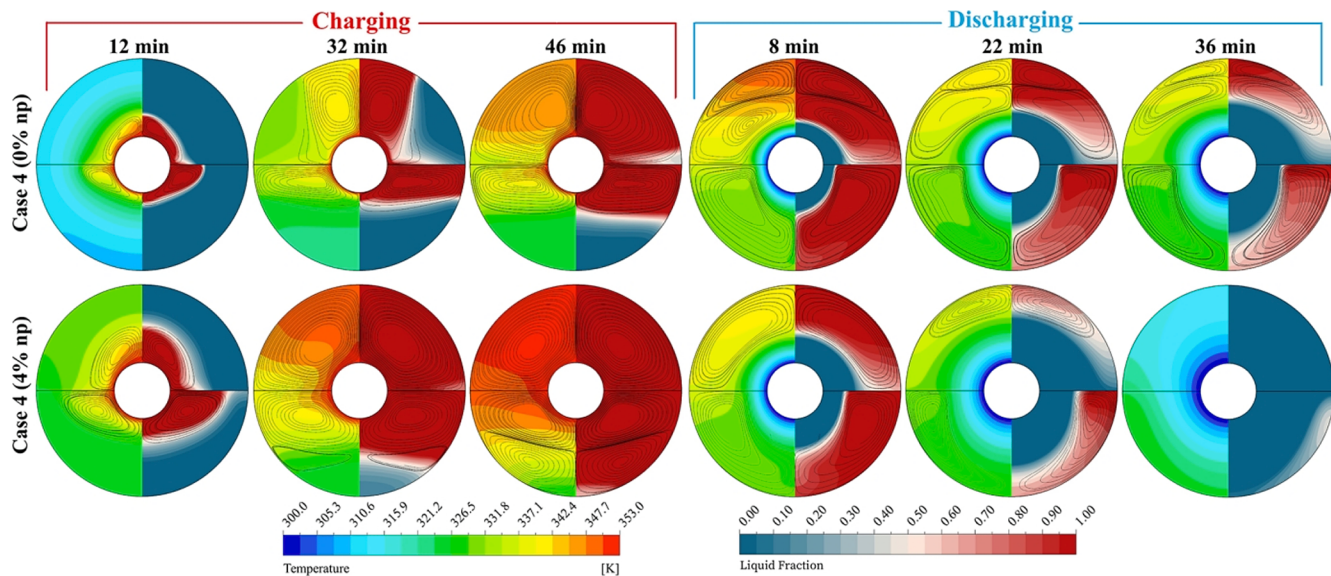


Fig. 11. Evolutions of the solid–liquid interface (right halves), isotherms (left halves) and streamlines in charging and discharging process for the new design with and without nanoparticles.

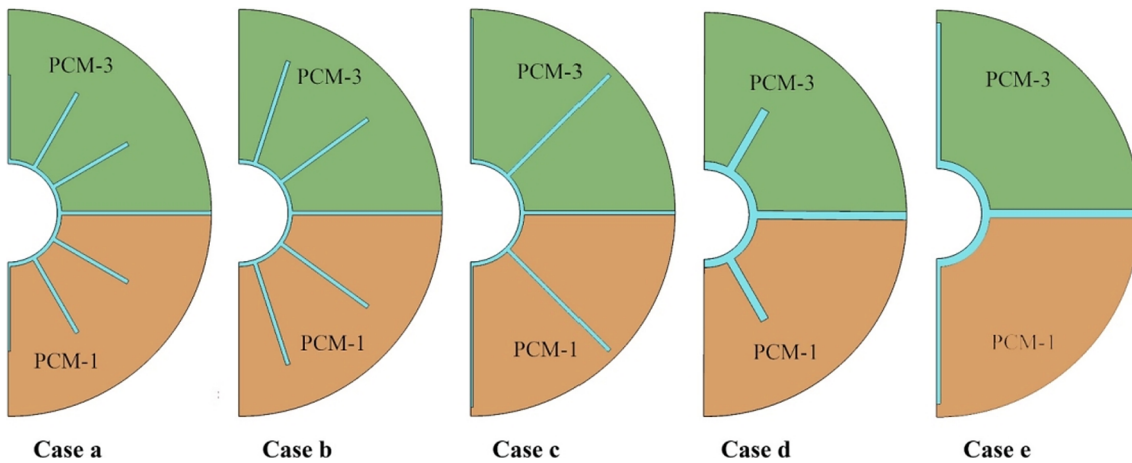


Fig. 12. Fin configurations applied for dual-PCM arrangement of case-4.

internal longitudinal fins, where both inner and outer tubes were subjected to a constant temperature of 65 °C was used to further validate our model. Fig. 3(b) shows that the results of this study corroborated with the experimental data reported in [46].

4.1.3. Verification of the model with nanoparticles

The numerical model is also verified by the numerical predictions of Khodadadi et al. [45] where copper nanoparticles were dispersed in water (as PCM) to improve its solidification rate in a differentially heated square cavity. Fig. 3 (c) compares the temporal liquid fraction results calculated by the currently developed model with those provided by Khodadadi et al. [45], demonstrating a strong coherence in results between both studies.

4.2. Grid and time-step independence

The effects of grid size and time step independence on the numerical predictions have been carefully examined (Fig. 4) for the dual-PCM configuration of case-4 (Fig. 2(d)). Fig. 4(a) demonstrates the latent stored energy for different grid sizes. As shown in Fig. 4(a), the differences in results between the case with 12,600 and 21,600 cells are small and negligible. Similarly, as Fig. 4(b) shows, halving a short time step of

0.1 s hardly changes the results, demonstrating that using 12,600 cells and 0.1 s time step is sufficient to produce reliable results.

5. Results and discussion

A total of 6 cases with different configurations of PCMs (refer to Fig. 2) are studied in this current work. The design development flowchart of the current study is presented in Fig. 5. Each stage is further discussed in the following sections.

5.1. Comparison of PCM configurations

5.1.1. Physical interpretation of the phenomena

Fig. 6 presents the solid–liquid interfaces and streamlines during the charging and discharging of the current TES unit for all cases depicted in Fig. 2. For each PCM configuration, it can be observed that the density variation of the liquid PCM causes upward liquid motions above the hot tube. Streamlines clearly show buoyancy effects, and recirculation regions are formed above the HTF tube. As a result, the upper zone experiences stronger natural convection-induced motions than the lower half. For instance, the liquid fraction for case 1, as demonstrated in Fig. 5, shows a skewed distribution at 50 min, and while the upper half is

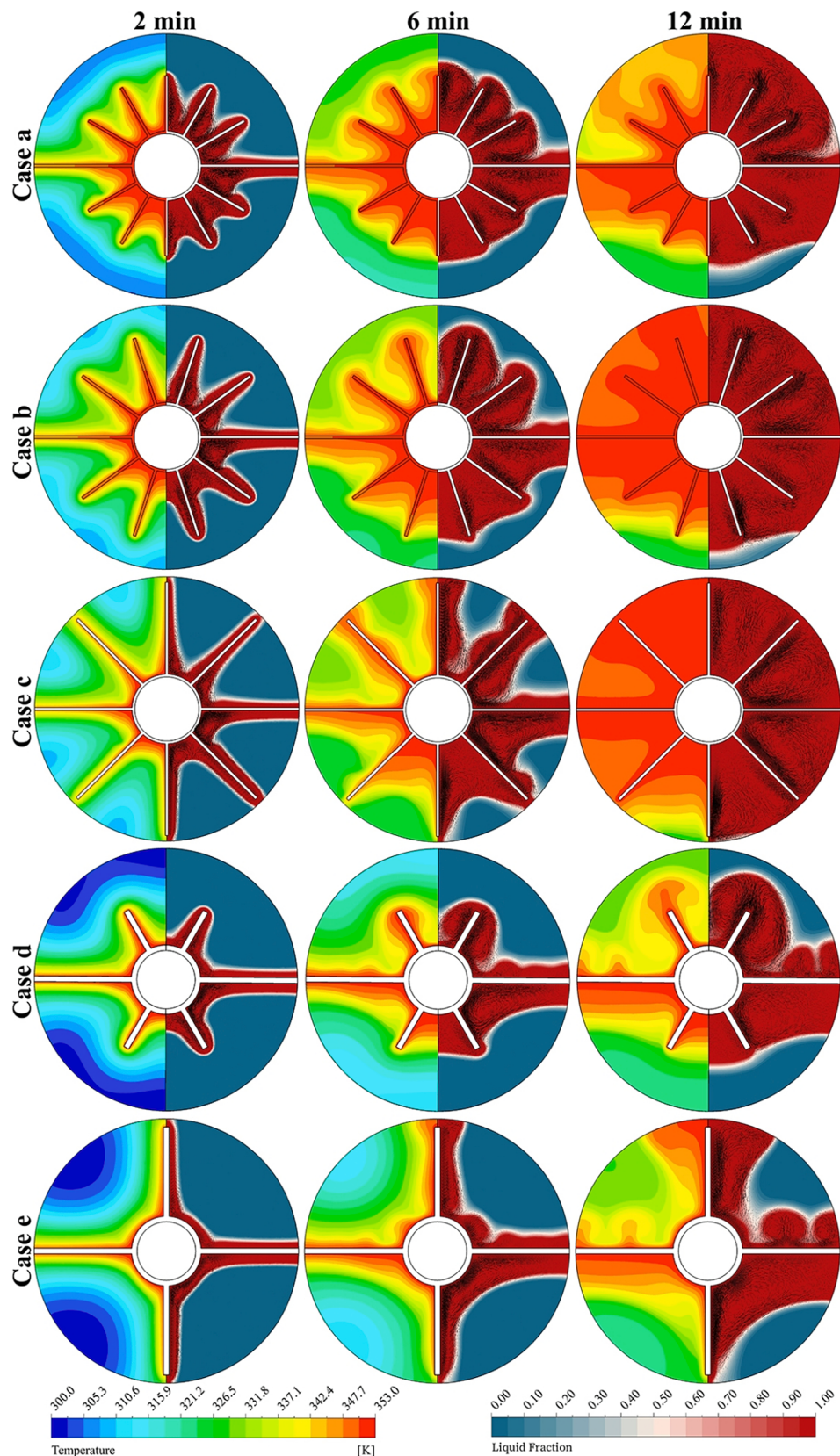


Fig. 13. Evolutions of solid–liquid interface, velocity vectors (right half) and isotherms (left half) for charging process of cases a, b, and c.

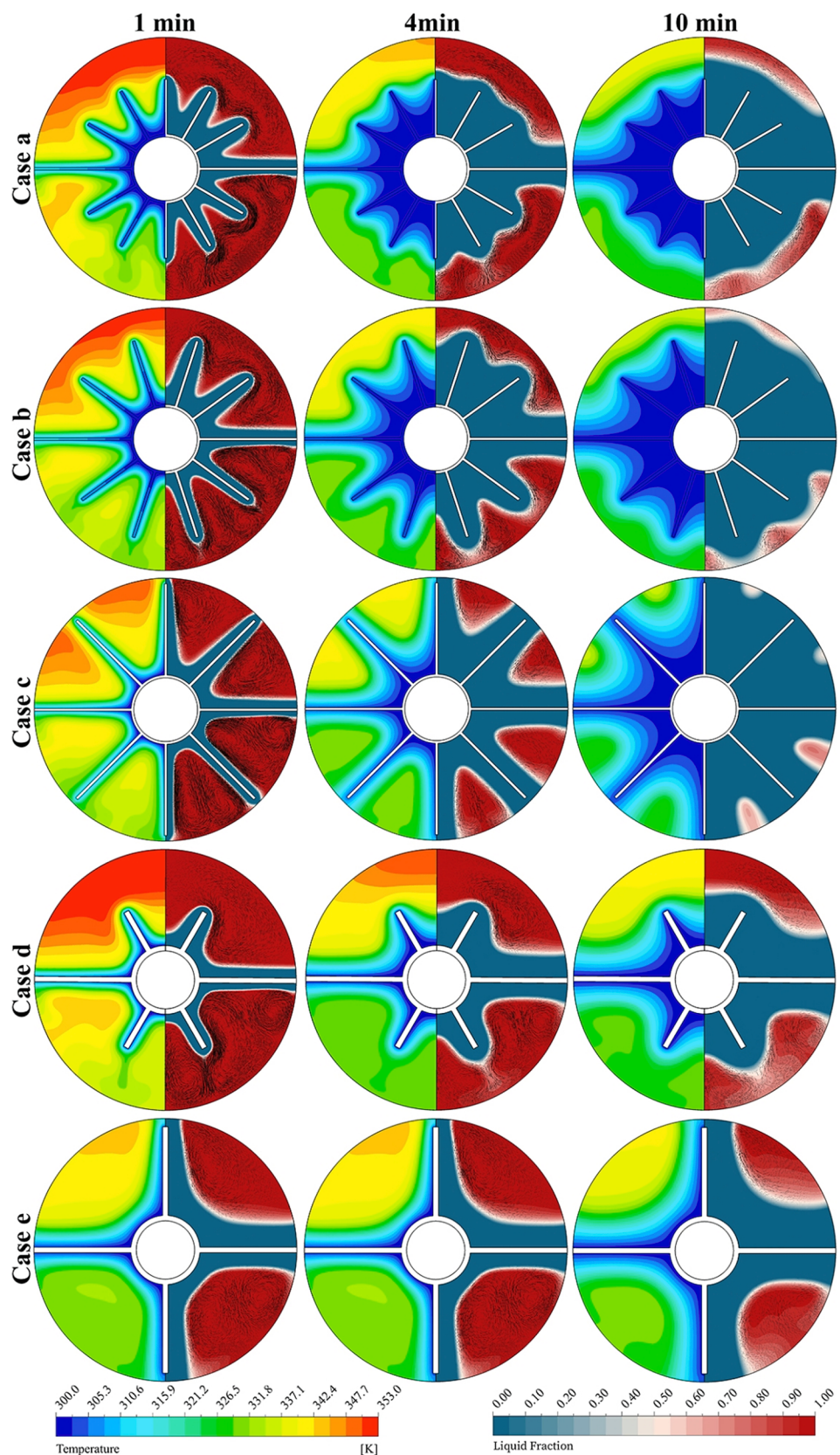


Fig. 14. Evolutions of solid-liquid interface, velocity vectors (right half) and isotherms (left half) for discharging process of cases a, b, and c.

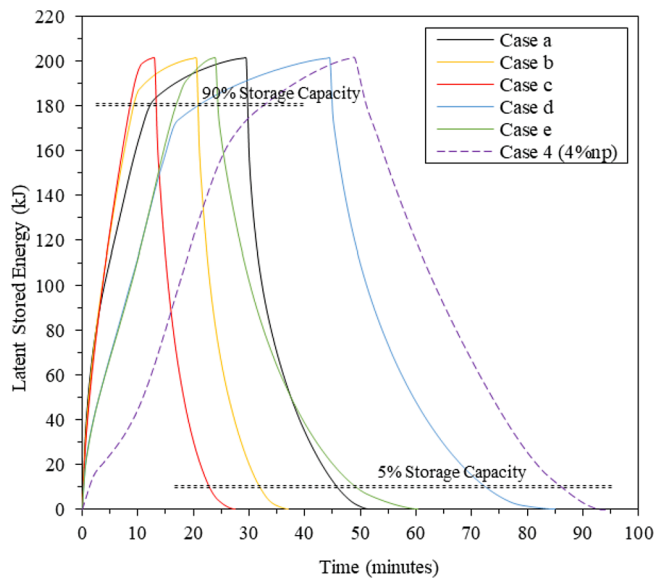


Fig. 15. Stored latent energy in consecutive charging and discharging of different fin configurations.

completely melted, only 39 % of the lower half is melted. However, weak natural convection is a benefit for discharging for this case, given that it appears to assist with accelerating the solidification process in the lower half (case-1 at Fig. 6). With case-2, where gravity effects are identical for both PCMs, PCM-1 (left side) has the quickest response in melting, while PCM-3 (right side) has the quickest solidification response, which can be explained using the difference between the pipe temperature and melting/solidification temperature of each PCM.

As mentioned above, in the lower half of the unit (more specifically in case-1 with a single PCM), the melting (charging) process is delayed,

while the upper half shows a slower response to solidification (discharging). Thus, if the upper zone is filled with a PCM (PCM-3) that solidifies quickly and the lower half is filled with a fast-melting PCM (PCM-1), a more uniform rate of melting and solidification could be attained in the upper and lower halves of the unit (case-4 at Fig. 6). After 50 min of charging, 64 % of the lower half in case-4 is melted, which is the highest among the cases. The reversed arrangement of PCMs (case-3: PCM-1 in the upper zone and PCM-3 in the lower zone) achieves the longest melting and solidification in the lower and upper halves, respectively.

Fig. 6 also shows that placements of PCMs in separate annulus-shaped sections (case-5 and case-6) don't lead to a fast melting. However, the arrangement of PCMs in case-6 leads to a fast solidification process since PCM-1 is placed around the cold tube, where the cold temperature at this area will compensate its delayed solidification.

Fig. 7 presents the transient change of isotherms for all applied configurations of the current TES unit in both charging and discharging periods. It is observed that isotherms are meaningfully deformed by convection-induced vortexes in the upper zone during the charging period. On the other hand, as shown in Fig. 7, during the discharging period (specifically for case-1), isotherms are mostly shaped like parallel distorted rings, indicating the dominance of the conduction heat transfer mechanism in the solidification process. Fig. 7 illustrates a significant temperature difference between the upper and lower halves of the annulus for all cases. This is due to the buoyancy effect of melted PCMs that causes upward movements of the hot liquid PCM. On the other hand, poor thermal conductivity of PCMs causes a significant temperature difference along the radial direction. It can be observed that arrangement of PCMs based on case-4 leads to a better temperature homogeneity compared with the other cases.

5.1.2. Heat transfer analysis

Fig. 8 presents the temporal evolution of the stored latent energy for the consecutive charging and discharging of the single PCM baseline

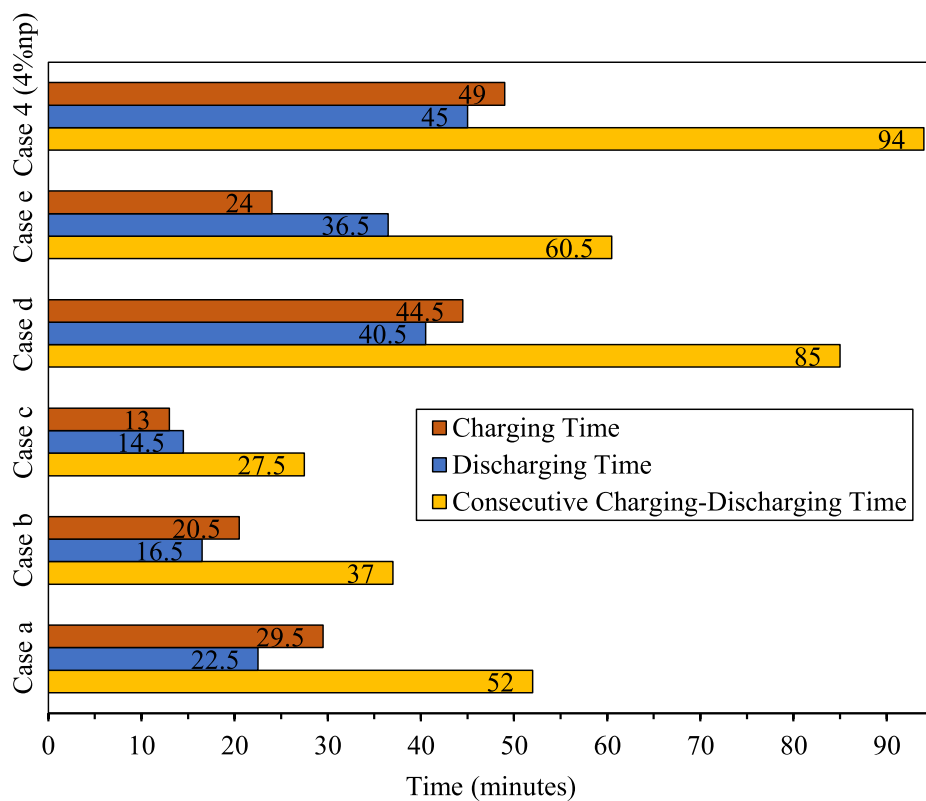


Fig. 16. Charging and discharging times for different cases, including 4% nanoparticles and fin configuration.

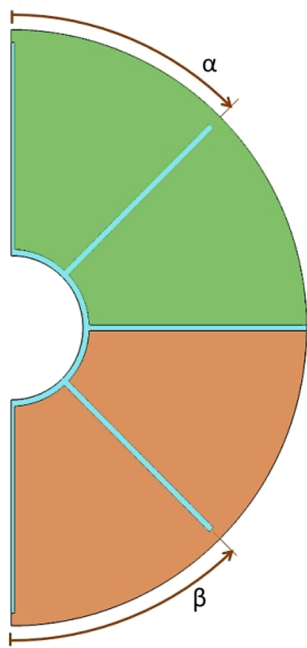


Fig. 17. Schematic of the long fin structure and angular parameters.

Table 2
Optimization parameters and their levels.

| Coded Symbol | Parameter ($^{\circ}$) | Level | | |
|--------------|--------------------------|---------------|--------------|---------------|
| | | 1 (coded: -1) | 2 (coded: 0) | 3 (coded: +1) |
| A | α | 15 | 45 | 75 |
| B | β | 15 | 45 | 75 |

Table 3
Design matrix and simulation response using central composite design.

| Run | Parameters | | Response t_t (s) |
|-----|-------------|------------|-----------------------|
| | A: α | B: β | |
| 1 | 15 | 45 | 2010 |
| 2 | 45 | 45 | 1650 |
| 3 | 45 | 15 | 1900 |
| 4 | 75 | 75 | 2240 |
| 5 | 45 | 75 | 2125 |
| 6 | 15 | 75 | 2700 |
| 7 | 15 | 15 | 2310 |
| 8 | 75 | 45 | 1695 |
| 9 | 75 | 15 | 2275 |

case and five different dual PCM design configuration cases. The length of the TES unit is considered to be 1 m so that the total energy can be calculated. As demonstrated in Fig. 8, case-4 renders the quickest thermal response and is the only effective dual-PCM configuration compared with the reference single PCM case (case-1). By applying the dual-PCM configuration of case-4, 13.6 % of the consecutive charging and discharging (CCD) time (33 min) is conserved compared with the reference case. Fig. 8 shows that the rate of energy storage declines significantly when 80 % of the capacity is utilized. A similar weakened trend could be observed in the discharging process when 10 % of the storage capacity remains in the system.

The required times for the full charging, discharging, and total charging-discharging are presented in Fig. 9 for all the six design configurations. Case-4 reveals the quickest responses in every period, where 17.2 % of the charging time (22 min), and 9.6 % of the discharging time (11 min) are conserved compared with the reference case. Fig. 9 shows

Table 4
ANOVA results for the current optimization.

| Source | Total time (t_t) | |
|-----------------------------------|----------------------|---------|
| | F-value | p-value |
| Model | 35.25 | 0.0072 |
| A | 22.54 | 0.0177 |
| B | 11.56 | 0.0425 |
| AB | 9.31 | 0.0554 |
| A^2 | 40.47 | 0.0079 |
| B^2 | 92.36 | 0.0024 |
| Standard deviation | | 69.65 |
| Mean | | 2100.56 |
| Coefficient of variation | | 3.32 |
| R^2 | | 0.9833 |
| $Adj. - R^2$ | | 0.9554 |
| Predicted R^2 | | 0.8631 |
| Adequate precision | | 19.7740 |

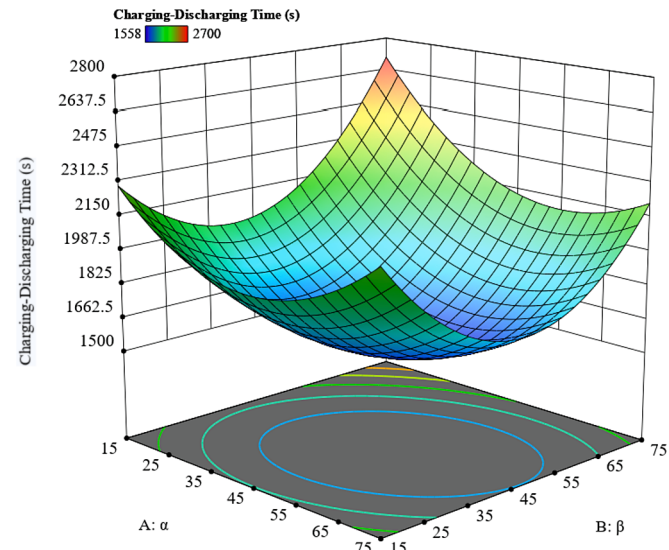


Fig. 18. Three-dimensional surface plot of total charging-discharging time based on design parameters (α and β).

that other dual-PCM arrangements (cases 2, 3, 5, and 6) are not better than the reference case in the CCD process. Explicitly, applying multiple PCMs may not necessarily lead to a better performance unless a proper configuration of PCMs is utilized to minimize the system's weaknesses in any specific condition.

Eq. (21) represents the storage heat contribution (SHR) in the TES system, which is the ratio of the latent stored energy to the maximum amount of latent energy that can be stored in the system (when the system is fully melted):

$$SHR = \frac{\text{Latent heat stored in the TES}}{\text{Heat storage capacity of TES}} \quad (21)$$

Temporal variation of SHR has been presented in Fig. 10 for all studied cases. The SHR share of each PCM has been identified with different colours. As expected, all dual-PCM configurations show different heat storage responses. For instance, for case-6 (Fig. 10(f)) from $t = 0$ to $t = 13$ min, only PCM-1 has contributed to energy storage since PCM-3 is placed far away from the HTF. As a result, the PCM-1 is fully melted after 70 min of charging, but the PCM-3 is fully melted after a long delay and after 138 min of charging. For case-3 (Fig. 10(c)), PCM-1 has been fully melted after 38 min which appears to have benefited from its low melting point and its location (being in the upper half with strong natural convection motions). On the contrary, PCM-3 lags in melting (141 min). As anticipated, PCM-3 solidifies more rapidly during

discharge due to its location and high solidification point (high-temperature difference between the cold pipe and solidus point). As a result, case-3 has the worst performance in CCD.

The best performance is observed with case-4 (Fig. 10(d)) where both PCMs have melted and solidified similarly with almost the same rates. In fact, the effective arrangement of PCMs in case-4 results in almost similar melting and solidification rates at different storage unit locations. Specifically, the delayed melting or solidification in blind regions is improved.

5.2. Further improvements in the performance of the new design

Having quick responses in storing and retrieving energy is crucial for TES systems. As discussed in section 5.1, case-4 renders the quickest CCD response among other cases. The suggested design could be further improved using thermal conductivity enhancers. The fixed volume fraction of 4 % has been considered for both nanoparticles and fin structures. Higher volume fractions are not examined to prevent further reduction in storage capacity or volume of PCM.

5.2.1. Effect of adding nanoparticles

In this section, the effect of dispersing Al_2O_3 nanoparticles (with a 4 % volume fraction at each PCM zone) has been examined on the CCD performance of the new dual-PCM design (case-4).

Fig. 11 compares the new design's graphical results (isotherms, solid–liquid interfaces, and streamlines) with pure PCMs and nanoparticle-enhanced PCMs. As observed, adding nanoparticles significantly enhances the phase change rate in the melting and solidification processes. This is expected as the thermal conductivity of NEPCMs is higher than those of the PCMs. However, the gain is more substantial when heat is mainly conducted, especially in the lower half of the system and while discharging (solidification).

5.2.2. Effect of adding fins

In this section, the effects of adding fins on the thermal performance of the new dual-PCM design (case-4) are investigated. To enable a reliable comparison, a fixed volume fraction of 4 % for all fin structures (same as the nanoparticles) is considered. In addition, fin thickness values of 0.5 mm (for cases a, b, and c) and 1 mm (for cases d and e) are studied. Fig. 12 shows the fin configurations examined in this study. In all of these configurations, horizontally extended fins have been devised to separate the upper and lower halves of the unit. As shown in Fig. 12, the number of fins, length and thickness of fins varied significantly in the five different design configurations.

Fig. 13 presents the liquid fraction and temperature variations of different fin structures during the charging process. The evolution of solid–liquid interfaces shows that case-c (with long thin fins) provides the fastest melting among the fin configurations, while case-d (with short thick fins) has the slowest melting. After 12 min of charging, the overall liquid fractions of 0.896, 0.956, 0.998, 0.658, and 0.656 are reported for the cases of a–e, respectively. The isotherms (Fig. 13, left halves) clearly show how high conductivity metal fins could distribute the heat from the HTF pipe wall throughout the space and accelerate the melting process.

The liquid fraction and isotherms of different fin structures during the discharge process are presented in Fig. 14. The graphical contours are presented after 1, 4, and 10 min of discharging for all the fin configurations. The discharging period commenced immediately after the fully melted (total liquid fraction of 1) condition. According to Fig. 14, case-c shows the quickest solidification response among the cases. After 10 min discharging, the overall liquid fractions of 0.185, 0.081, 0.043, 0.377, and 0.349 are reported for the cases of a–e, respectively. The evolution of isotherms shows that long thin fins could provide a better temperature distribution leading to a fast solidification process.

5.2.3. Heat transfer comparison of fins and nanoparticles

Fig. 15 presents the temporal stored latent heat in consecutive charging and discharging cycles when different fin structures, and nanoparticles, are applied. As observed, adding 4 % fin is more effective than adding 4 % nanoparticles to the optimum dual-PCM configuration. Applying nanoparticles to the new dual-PCM design leads to a 2.2 times shorter CCD process, while adding fins leads to 2.5–7.6 times shorter CCD processes. Case-c with long thin fins (and a smaller number of fins) provides the best and quickest response in the whole charging-discharging process. Fig. 15 shows that the rate of energy storage significantly declines when about 90 % of the storage capacity is utilized. The reason behind this behaviour is that the lower region of the storage unit lacks strong natural convection-induced motions. Thus, having long fins at the lower region leads to higher gradients which could be seen for case-c and case-e. A similar weakened trend could be seen in the discharging (solidification) process when 5 % of the storage capacity is remained, which is associated with a strong natural convection effect in the upper region (leading to delayed solidification in this region). Therefore, optimising fin angles (for case-c with long fins and quicker performance) could promote better performance.

The charging, discharging, and total times of studied cases have been summarized in Fig. 16. Note that case-c reveals the quickest times in every process. Furthermore, applying thin fins (with 0.5 mm thickness) results in faster responses compared to fins with a thickness of 1 mm. The charging and discharging periods have been shortened by up to 8.15 times and 7.17 times by applying the configuration of case-c (compared with the baseline case-4 without fins or nanoparticles).

5.2.4. Fin optimization

In this section, the geometrical parameters of the best fin structure (case-c) are optimized using Response Surface Methodology (RSM). RSM has been widely used as an effective method to optimize and determine the functional correlation of input parameters [47]. As depicted in Fig. 17, the angles of oblique fins (α and β) are selected to be optimized, whereas the total charging-discharging time (t_t) has been selected as the objective function to be minimized. The ranges of optimization parameters are listed in Table 2. The design optimization approach can be expressed as:

$$\left\{ \begin{array}{l} \text{Find } \alpha, \beta \\ \text{Evaluate } t_t = f\{\alpha, \beta\} \\ \text{Minimize } f = t_t \\ \text{Subject to :} \\ 15 \leq \alpha \leq 75 \\ 15 \leq \beta \leq 75 \end{array} \right. \quad (22)$$

The design of experiment (DOE) is adopted for the regression analysis, which could develop a functional relationship between the desired response, y , and independent input parameters, which affect the system response denoted as X_1, X_2, \dots, X_i . A second-order polynomial model was implemented, which is capable of predicting the combined effect of design parameters on the desired response. A second-order polynomial model can be expressed as:

$$y = b_0 + \sum_{i=1}^n b_i x_i + \sum_{i=1}^n b_{ii} x_i^2 + \sum_{i < j}^n b_{ij} x_i x_j \pm \varepsilon \quad (23)$$

In the abovementioned equation, y is the desired response, n is the number of design parameters, x_i is the independent design parameter, ε is the fitting error, b_0 is a constant while b_i , b_{ii} and b_{ij} are coefficients of linear, second degree and mixed terms of the model, respectively.

Central composite design was utilized to generate design points and test the quadratic model's fitness. Nine simulations were performed to obtain the responses, which are presented in Table 3. The RSM was utilized to build polynomial model for the response. The second-order regression model made for the response (t_t) based on coded values for the current optimization study could be expressed as:

$$t_r = +1576.11 - 135A + 96.67B - 106.25AB + 313.33A^2 + 473.33B^2 \quad (24)$$

Equation (24) shows that both parameters significantly affect the predicted total time, however factor A (α) has a higher effect on the response due to its higher coefficient.

Analysis of variance (ANOVA) was utilized to determine the significance and adequacy of the model with the result summarized in Table 4. It could be seen that the p -value is less than 0.05, indicating the significance of the current second-order polynomial model. Table 4 presents R^2 and $Adj-R^2$ values as 0.9833, and 0.9554, respectively, indicating good fitting of the actual and predicted results in predicting the total charging-discharging time for the selected configuration. Furthermore, Table 4 presents an adequate value of 19.77. This value measures the signal to noise ratio, and a value higher than 4 indicates high signal to noise ratio.

Fig. 18 shows the three-dimensional surface representing the response (t_r), based on the optimization parameters (α and β), which are also described in the equation (24). As observed, good results (low values of total charging-discharging time) could be achieved when α and β are selected almost in the middle range. Furthermore, a combination of the minimum angle of the upper fin (minimum α) and the maximum angle of the lower fin (maximum β) leads to the worst condition (maximum value of t_r). The optimization results suggested that the optimum design can be achieved when $\alpha = 51.1^\circ$ and $\beta = 42.6^\circ$, where the total charging-discharging time is predicted as 1558.6 s. This recommended design has been validated with the numerical model where only 2.2 % relative deviation is observed, indicating the reliability of the RSM results. The optimized design decreased the total charging-discharging time up to 7.5 % compared with the baseline design (case-c).

6. Conclusion

This paper proposed an innovative fin-structured dual-PCM thermal energy storage system to improve the charging and discharging of horizontal heat storage units. To the best of the authors knowledge, the combined benefits of fins and dual-PCMs have not been explored, and there is no reported work to suggest an efficient dual-PCM layout that facilitates both melting and solidification processes. Consecutive melting and solidification have been compared between 6 different arrangements of dual-PCM in a horizontal double-tube heat exchanger. The results indicate that placing a PCM with a lower melting point at the lower half and a PCM with a higher melting point at the upper half of the storage unit can significantly improve both melting and solidification processes. The entire charging-discharging process is accelerated by 13.6 % (33 min shorter) than the baseline case (single PCM), and a more uniform rate of phase change is observed in different parts of the storage unit with dual-PCMs setup. Further improvement of the proposed design has been investigated by adding different fin structures as well as Al_2O_3 nanoparticles.

The graphical results of the numerical model for a single-PCM storage unit show that the natural convection effect at the upper half is much higher than the lower half due to uprising movements of hot melted PCMs with lesser density. This leads to a delayed charging of the lower zone and a delayed discharging of the upper zone. However, applying an optimum dual-PCM arrangement (low-melting-point PCM at the lower half and high-melting-point PCM at the upper zone) significantly improves this non-uniformity, leading to improvement in the charging-discharging process.

The effects of adding Al_2O_3 nanoparticles and different fin structures (with different fin numbers, thicknesses and lengths) with low volume concentration (4 %) have been investigated on the charging and discharging performance of the proposed dual-PCM design (case-4). Adding fins is found to be more effective than adding nanoparticles. The results show that adding elongated thin fins can achieve the quickest charging and discharging duration, which is 7.6 times shorter than the proposed dual-PCM design without fins.

By suggesting a structure with elongated thin fins, the angles of oblique fins at lower and upper zones (α and β) are optimized using RSM. The optimum angles of $\alpha = 51.1^\circ$ and $\beta = 42.6^\circ$ are suggested to provide the quickest performance, which is 7.5 % shorter than the baseline design (case-c: best fin structure with equally spaced fins). This study provided guidelines to maximize the performance enhancement of a double-pipe energy storage unit for both charging and discharging mechanisms where only a small portion of the storage capacity is occupied by fins.

CRediT authorship contribution statement

M. Mozafari: Conceptualization, Methodology, Investigation, Validation, Software, Formal analysis, Data curation, Writing – original draft, Writing – review & editing, Project administration, Resources. **Kamel Hooman:** Supervision, Formal analysis, Writing – review & editing. **Ann Lee:** Supervision, Writing – review & editing. **Shaokoon Cheng:** Supervision, Writing – review & editing.

Declaration of Competing Interest

The authors declare that they have no known competing financial interests or personal relationships that could have appeared to influence the work reported in this paper.

Data availability

Data will be made available on request.

References

- [1] F. Martins, C. Felgueiras, M. Smitkova, N. Caetano, Analysis of fossil fuel energy consumption and environmental impacts in European countries, *Energies* 12 (2019) 964.
- [2] M. Mozafari, A. Lee, S. Cheng, A novel dual-PCM configuration to improve simultaneous energy storage and recovery in triplex-tube heat exchanger, *Int. J. Heat Mass Transf.* 186 (2022), 122420.
- [3] R. Chaturvedi, A. Islam, K. Sharma, A review on the applications of PCM in thermal storage of solar energy, *Mater. Today.: Proc.* 43 (2021) 293–297.
- [4] K. Du, J. Calautit, P. Eames, Y. Wu, A state-of-the-art review of the application of phase change materials (PCM) in Mobilized-Thermal Energy Storage (M-TES) for recovering low-temperature industrial waste heat (IWH) for distributed heat supply, *Renewable Energy* 168 (2021) 1040–1057.
- [5] M. Mozafari, A. Lee, J. Mohammadpour, Thermal Management of Single and Multiple PCMs based Heat Sinks for Electronics Cooling, *Thermal Science and Engineering Progress* 23 (2021) 100919, <https://doi.org/10.1016/j.tsep.2021.100919>.
- [6] M. Mozafari, A. Lee, S. Cheng, Improvement on the cyclic thermal shock resistance of the electronics heat sinks using two-objective optimization, *J. Storage Mater.* 46 (2022), 103923.
- [7] J. Luo, D. Zou, Y. Wang, S. Wang, L. Huang, Battery thermal management systems (BTMs) based on phase change material (PCM): A comprehensive review, *Chem. Eng. J.* 430 (2022), 132741.
- [8] F. Yi, J. E, B. Zhang, H. Zuo, K. Wei, J. Chen, H. Zhu, H. Zhu, Y. Deng, Effects analysis on heat dissipation characteristics of lithium-ion battery thermal management system under the synergism of phase change material and liquid cooling method, *Renewable Energy* 181 (2022) 472–489.
- [9] M. Faizan, R. Ahmed, H.M. Ali, A critical review on thermophysical and electrochemical properties of iononfluids (nanoparticles dispersed in ionic liquids) and their applications, *J. Taiwan Inst. Chem. Eng.* 124 (2021) 391–423.
- [10] A. Mourad, A. Aissa, F. Mebarek-Oudina, W. Jamshed, W. Ahmed, H.M. Ali, A. Rashad, Galerkin finite element analysis of thermal aspects of Fe3O4-MWCNT/water hybrid nanofluid filled in wavy enclosure with uniform magnetic field effect, *Int. Commun. Heat Mass Transfer* 126 (2021), 105461.
- [11] M. Saleem, A. Algahtani, S.U. Rehman, M.S. Javed, K. Irshad, H.M. Ali, M.Z. Malik, A. Ali, V. Tirth, S. Islam, Solution processed $Zn1-x-ySmxCuY$ nanorod arrays for dye sensitized solar cells, *Nanomaterials* 11 (2021) 1710.
- [12] A. Ali, F.A. Al-Sulaiman, I.N. Al-Duais, K. Irshad, M.Z. Malik, M. Shafiullah, M. Zahir, H.M. Ali, S.A. Malik, Renewable portfolio standard development assessment in the Kingdom of Saudi Arabia from the perspective of policy networks theory, *Processes* 9 (2021) 1123.
- [13] A.M. Abdulateef, S. Mat, J. Abdulateef, K. Sopian, A.A. Al-Abidi, Geometric and design parameters of fins employed for enhancing thermal energy storage systems: a review, *Renew. Sustain. Energy Rev.* 82 (2018) 1620–1635.
- [14] M. Mozafari, M.A. Akhavan-Behabadi, H. Qobadi-Arfaee, M. Fakoor-Pakdaman, Condensation and pressure drop characteristics of R600a in a helical tube-in-tube

- heat exchanger at different inclination angles, *Appl. Therm. Eng.* 90 (2015) 571–578.
- [15] M. Mozafari, M.A. Akhavan-Behabadi, H. Qobadi-Arfaee, P. Hanafizadeh, M. Fakoor-Pakdaman, Experimental study on condensation flow patterns inside inclined U-bend tubes, *Exp. Therm Fluid Sci.* 68 (2015) 276–287.
- [16] C. Zhao, M. Opolot, M. Liu, F. Bruno, S. Mancin, K. Hooman, Phase change behaviour study of PCM tanks partially filled with graphite foam, *Appl. Therm. Eng.* 196 (2021), 117313.
- [17] S. Rostami, M. Afrand, A. Shahsavari, M. Sheikholeslami, R. Kalbasi, S. Aghakhani, M.S. Shadloo, H.F. Oztop, A review of melting and freezing processes of PCM/nano-PCM and their application in energy storage, *Energy* 211 (2020), 118698.
- [18] A. Pizzolato, A. Sharma, K. Maute, A. Sciacovelli, V. Verda, Design of effective fins for fast PCM melting and solidification in shell-and-tube latent heat thermal energy storage through topology optimization, *Appl. Energy* 208 (2017) 210–227.
- [19] M. Nakhchi, J. Esfahani, Improving the melting performance of PCM thermal energy storage with novel stepped fins, *J. Storage Mater.* 30 (2020), 101424.
- [20] J. Guo, Z. Liu, B.o. Yang, X. Yang, J. Yan, Melting assessment on the angled fin design for a novel latent heat thermal energy storage tube, *Renewable Energy* 183 (2022) 406–422.
- [21] A. Sharma, P. Parth, S. Shobhana, M. Bobin, B. Hardik, Numerical study of ice freezing process on fin aided thermal energy storage system, *Int. Commun. Heat Mass Transfer* 130 (2022), 105792.
- [22] S. Yao, X. Huang, Study on solidification performance of PCM by longitudinal triangular fins in a triplex-tube thermal energy storage system, *Energy* 227 (2021), 120527.
- [23] J. Zheng, J. Wang, T. Chen, Y. Yu, Solidification performance of heat exchanger with tree-shaped fins, *Renewable Energy* 150 (2020) 1098–1107.
- [24] J.M. Mahdi, F.T. Najim, I.M. Aljubury, H.I. Mohammed, N.B. Khedher, N. Alshammari, A. Cairns, P. Talebizadehsardari, Intensifying the thermal response of PCM via fin-assisted foam strips in the shell-and-tube heat storage system, *J. Storage Mater.* 45 (2022), 103733.
- [25] Y. Huang, F. Yao, X. Liu, Numerical study on the thermal enhancement of horizontal latent heat storage units with hierarchical fins, *Renewable Energy* 180 (2021) 383–397.
- [26] J.M. Mahdi, H.I. Mohammed, E.T. Hashim, P. Talebizadehsardari, E.C. Nsofor, Solidification enhancement with multiple PCMs, cascaded metal foam and nanoparticles in the shell-and-tube energy storage system, *Appl. Energy* 257 (2020), 113993.
- [27] I. Al Siyabi, S. Khanna, T. Mallick, S. Sundaram, Experimental and numerical study on the effect of multiple phase change materials thermal energy storage system, *J. Storage Mater.* 36 (2021), 102226.
- [28] M. Mozafari, A. Lee, S. Cheng, Simulation Study of Solidification in the Shell-And-Tube Energy Storage System with a Novel Dual-PCM Configuration, *Energies* 15 (2022) 832.
- [29] M. Mozafari, A. Lee, S. Cheng, Simultaneous energy storage and recovery in triplex-tube heat exchanger using multiple phase change materials with nanoparticles, *J. Storage Mater.* 49 (2022), 104164.
- [30] A.A. Al-Abidi, S. Mat, K. Sopian, M.Y. Sulaiman, A.T. Mohammad, Experimental study of melting and solidification of PCM in a triplex tube heat exchanger with fins, *Energy Build.* 68 (2014) 33–41.
- [31] A.A. Al-Abidi, S. Mat, K. Sopian, M.Y. Sulaiman, A.T. Mohammad, Numerical study of PCM solidification in a triplex tube heat exchanger with internal and external fins, *Int. J. Heat Mass Transf.* 61 (2013) 684–695.
- [32] J.M. Mahdi, S. Lohrasbi, D.D. Ganji, E.C. Nsofor, Simultaneous energy storage and recovery in the triplex-tube heat exchanger with PCM, copper fins and Al₂O₃ nanoparticles, *Energy Convers. Manage.* 180 (2019) 949–961.
- [33] J.M. Mahdi, E.C. Nsofor, Solidification of a PCM with nanoparticles in triplex-tube thermal energy storage system, *Appl. Therm. Eng.* 108 (2016) 596–604.
- [34] Rubitherm GmbH, <https://www.rubitherm.eu>.
- [35] A.A. Rabienataj Darzi, M. Jourabian, M. Farhadi, Melting and solidification of PCM enhanced by radial conductive fins and nanoparticles in cylindrical annulus, *Energy Convers. Manage.* 118 (2016) 253–263.
- [36] L. Pu, S. Zhang, L. Xu, Z. Ma, X. Wang, Numerical study on the performance of shell-and-tube thermal energy storage using multiple PCMs and gradient copper foam, *Renewable Energy* 174 (2021) 573–589.
- [37] M.M. Prieto, B. González, Fluid flow and heat transfer in PCM panels arranged vertically and horizontally for application in heating systems, *Renewable Energy* 97 (2016) 331–343.
- [38] H.M. Sadeghi, M. Babayan, A. Chamkha, Investigation of using multi-layer PCMs in the tubular heat exchanger with periodic heat transfer boundary condition, *Int. J. Heat Mass Transf.* 147 (2020), 118970.
- [39] R.S. Vajjha, D.K. Das, Experimental determination of thermal conductivity of three nanofluids and development of new correlations, *Int. J. Heat Mass Transf.* 52 (21–22) (2009) 4675–4682.
- [40] R.S. Vajjha, D.K. Das, P.K. Namburu, Numerical study of fluid dynamic and heat transfer performance of Al₂O₃ and CuO nanofluids in the flat tubes of a radiator, *Int. J. Heat Fluid Flow* 31 (4) (2010) 613–621.
- [41] A.V. Arasu, A.S. Mujumdar, Numerical study on melting of paraffin wax with Al₂O₃ in a square enclosure, *Int. Commun. Heat Mass Transfer* 39 (1) (2012) 8–16.
- [42] A. Brent, V.R. Voller, K. Reid, Enthalpy-porosity technique for modeling convection-diffusion phase change: application to the melting of a pure metal, *Numerical Heat Transfer, Part A Applications* 13 (1988) 297–318.
- [43] B.P. Leonard, A stable and accurate convective modelling procedure based on quadratic upstream interpolation, *Comput. Methods Appl. Mech. Eng.* 19 (1) (1979) 59–98.
- [44] S. Patankar, Numerical heat transfer and fluid flow, Taylor & Francis, 2018.
- [45] J.M. Khodadadi, S.F. Hosseini-Zadeh, Nanoparticle-enhanced phase change materials (NEPCM) with great potential for improved thermal energy storage, *Int. Commun. Heat Mass Transfer* 34 (5) (2007) 534–543.
- [46] A.M. Abdulateef, J. Abdulateef, S. Mat, K. Sopian, B. Elhub, M.A. Mussa, Experimental and numerical study of solidifying phase-change material in a triplex-tube heat exchanger with longitudinal/triangular fins, *Int. Commun. Heat Mass Transfer* 90 (2018) 73–84.
- [47] G. Box, K. Wilson, Experimental designs for exploring response surfaces, *Ann Math Stat* 13 (1951) 1–45.